Acta Oceanol. Sin., 2021, Vol. 40, No. 1, P. 70–84
https://doi.org/10.1007/s13131-021-1702-9
http://www.hyxb.org.cn
E-mail: hyxbe@263.net

Observational study of super typhoon Meranti (2016) using satellite, surface drifter, Argo float and reanalysis data

Hui Chen[1], Shuang Li[1]*, Hailun He[2], Jinbao Song[1], Zheng Ling[3], Anzhou Cao[1], Zhongshui Zou[1], Wenli Qiao[1]

[1] Ocean College, Zhejiang University, Zhoushan 316021, China

[2] State Key Laboratory of Satellite Ocean Environment Dynamics, Second Institute of Oceanography, Ministry of Natural Resources, Hangzhou 310012, China

[3] Key Laboratory of Coastal, Resources and Environment in Continental and Deep Sea of Department of Education of Guangdong Province, Guangdong Ocean University, Zhanjiang 524088, China

Received 15 September 2019; accepted 5 March 2020

Abstract

The present work describes the basic features of super typhoon Meranti (2016) by multiple data sources. We mainly focus on the upper ocean response to Meranti using multiplatform satellites, *in situ* surface drifter and Argo floats, and compare the results with the widely used idealized wind vortex model and reanalysis datasets. The pre-existing meso-scale eddy provided a favor underlying surface boundary condition and also modulated the upper ocean response to Meranti. Results show that the maximum sea surface cooling was 2.0°C after Meranti. The satellite surface wind failed to capture the core structure of Meranti as the idealized wind vortex model deduced. According to the observation of sea surface drifters, the near-inertial currents were significantly enhanced during the passage of Meranti. The temperature and salinity profiles from Argo floats revealed both the mixed-layer extension and subsurface upwelling induced by Meranti. The comparison results show that the sea surface temperature and surface wind in the reanalysis datasets differs from those in remote sensing system. Sea surface cooling is similar in both satellite and *in situ* observation, and sea surface salinity response has a lower correlation with the precipitation rate.

Key words: super typhoon, satellite data, sea surface temperature, surface wind

Citation: Chen Hui, Li Shuang, He Hailun, Song Jinbao, Ling Zheng, Cao Anzhou, Zou Zhongshui, Qiao Wenli. 2021. Observational study of super typhoon Meranti (2016) using satellite, surface drifter, Argo float and reanalysis data. Acta Oceanologica Sinica, 40(1): 70–84, doi: 10.1007/s13131-021-1702-9

1 Introduction

Tropical cyclone (TC) is an extreme event in the coupled atmosphere and ocean system, which is commonly regarded as a natural disaster in human society (Emanuel, 2003; Zhang et al., 2009). As the top class of TC, each super typhoon is worth comprehensively studying to improve the present understanding of TC events.

Typhoon observations are primarily achieved by satellites (Guan et al., 2017; Yue et al., 2018; Jin et al., 2019). Satellite is an important reconnaissance platform for the determination of best track (Cassity and Colgan, 1973). Generally, at the cyclogenesis phase, cloud patterns in satellite imagery indicate the existence of TC. Later after TC reaches tropical storm intensity, the TC intensity changes are correlated with cloud features (Velden et al., 2006). Based on multi-platform reconnaissance datasets, interpolating in the temporal and spatial grids lead to quantitative estimation of TC position, size, and intensity (Knaff et al., 2010).

Satellite-retrieved sea surface temperature (SST), surface wind, and precipitation data are frequently used to describe TC events. Indeed, these three parameters all contribute to the TC energy balance. First, SST determines the air-sea turbulent heat flux (latent and sensible heat fluxes), and warmer SST provides favorable conditions for TC development (Cione, 2015; Sun et al., 2019). Second, surface wind is a realization of the mechanical energy transferred from the TC. Surface wind and surface turbulent heat flux play different roles in TC dynamics, and they are the sink and source of TC energy, respectively. Third, the precipitation represents the latent heat release from water vapor and supplies considerable energy for the development of a TC (Adler and Rodgers, 1977). In light of these knowledge, satellite products provide indispensable information for the study and operational forecast of TC events.

SST can be retrieved from visible infrared and microwave satellite sensors (Kishtawal, 2016). As an infra sensor, the advanced very high resolution radiometer (AVHRR) has high precision, but the data are limited to cloud-free conditions. Passive microwave sensors, such as the special sensor microwave/imager (SSM/I) and the tropical rainfall measuring mission (TRMM) microwave imager (TMI), are not subject to the cloud coverage restriction and are supposed to have all-weather working capability. After *in situ* calibration, blended SST data (Reynolds et al., 2007) are suitable for operational weather monitoring

Foundation item: The National Program on Global Change and Air-Sea Interaction under contract No. GASI-IPOVAI-04, the National Natural Science Foundation of China under contract Nos 41830533, 41876003 and 41621064; the China-Sweden (NSFC-STINT) Cooperation and Exchange Project under contract No. 41911530149.
*Corresponding author, E-mail: lshuang@zju.edu.cn

(Fu et al., 2018).

For surface wind data, microwave radar scatterometers, such as Seasat, European remote-sensing-1 (ERS-1), European remote-sensing-2 (ERS-2), Quick Scatterometer (QuickSCAT), SeaWinds, and advanced scatterometer (ASCAT), can measure surface wind vectors (Hawkins and Black, 1983; Jones et al., 1999). However, scatterometers have proved problematic in rainy conditions, and the relationship between wind and the received signal is considerably weak in high-wind regimes; thus, scatterometers result in local deficiencies in observation fields. Further, so-called saturation leads to the underestimation of wind speed in high winds when using the empirical relationship in moderate wind conditions (Fu et al., 2018). Occasionally, scatterometers happen to scan the center of a TC and can describe the spatial structure of the TC core (Kishtawal, 2016). Passive microwave sensors, like SSM/I, TMI, and global precipitation measurement (GPM) microwave imager (GMI), are used to retrieve precipitation data. Since there is a close relationship between the rain rate and microwave radiation (or brightness temperature), precipitation is well measured from space platforms (Adler and Rodgers, 1977). Active microwave sensors, such as TRMM Precipitation Radar, provide three-dimensional rain rates during a TC, and this information is critical to the three-dimensional initial conditions of model-based weather forecasting. However, there is still room to improve the retrieval of remotely sensed observations on the core structure of typhoons. Obstacles to achieving a better understanding of these events include suboptimal temporal and spatial resolution, as well as the shielding effect of clouds. Furthermore, the calibration and evaluation of satellite data on marine surfaces are challenging because of insufficient *in situ* observations. Surface drifters and profiling floats are too sparse to resolve the horizontal structure of a TC.

In fact, in situ ocean observations remain largely based on chance. On the other hand, satellite and in situ observations are being increasingly integrated into data assimilation systems, in which a numerical model is used to pursue consistent datasets. The output data are referred to as analysis or reanalysis. One of the important applications of analysis/reanalysis data is their use as the initial conditions for numerical forecast and hindcast simulation. It is doubtless that the information from satellite and *in situ* observations is the backbone of reanalysis datasets, but the numerical model and data assimilation method also affect the analysis results. Among the limitations of satellite and *in situ* observations is the little information they yield about super typhoons (Guan et al., 2014; Cao et al., 2018; He et al., 2018). This restricts the reliability of atmospheric and oceanic reanalysis. Therefore, for super typhoon events, it is crucial to perform integrated studies that cover satellite data, *in situ* observations, and related analysis and reanalysis. The results of such research can serve as preliminary knowledge on a specific super typhoon and pave the road for the potential next-step model simulation (Li et al., 2016; Zhao et al., 2017; Sun et al., 2019).

The western North Pacific (WNP) experiences the highest occurrence of TCs in the world (Pun et al., 2011). On average, there are 16 typhoons per year, and they mainly occur in summer and autumn (Webster et al., 2005). The upper ocean response to tropical cyclones involves many mechanisms, including near-inertial current, near-inertial internal wave, sea surface cooling, vertical mixing, and subsurface upwelling (Price, 1981). When the moving speed of typhoon is faster than the phase speed of first baroclinic mode in the upper ocean (Chang et al., 2013), near-inertial currents were induced after the passage of typhoon, meanwhile, near-inertial internal waves were generated at the base of mixed-layer, and the corresponding mechanic energy propagated downward (Nilsson, 1995; Chen et al., 2015). Enhanced vertical mixing is related to the near-inertial current in the near surface, which is relatively strong on the right-hand side of a typhoon track as a result of the resonance effect. Subsurface upwelling is induced by Ekman transport.

Meanwhile, sea surface cooling significantly affects the air-sea sensible and latent heat fluxes and therefore has a negative feedback on TC intensity (Wada et al, 2014; Cione, 2015; Wada et al., 2018). The WNP is also characterized by mesoscale eddies, which modulate SST and affect the development of a TC (Qiu, 1999). The rapid intensification of a number of typhoons has been found to be related to warm core eddies (Hong et al., 2000; Shay et al., 2000).

Studying the characteristics of a specific super typhoon is of great scientific significance and a step toward understanding super typhoons in general. This paper focuses on super typhoon Meranti, which was a widely-impact disaster to Batanes, Taiwan, and Fujian in September 2016. This study aims to describe the basic features of super typhoon Meranti, investigate the ocean response to Meranti using multi-satellite and *in situ* ocean measurements, and evaluate the performance of related atmospheric and ocean reanalysis. In the next section we briefly introduce the data we used, the results are shown in Section 3. In Section 4 we discuss the performance of reanalysis datasets and how the pre-existing warm eddy modulate the typhoon-induced SST cooling, and the conclusions are given in the last section.

2 Data

2.1 *Best-track data*

The best-track data are the best estimation of the position and intensity of the TC based on various sources of available in situ and satellite observations. The best-track data include the location of TC center, the minimum pressure, the maximum sustained wind speed, the radius of maximum winds. The international best track archive for climate stewardship (IBTrACS) contains the most complete historical information about TCs around the globe (Knapp et al., 2010). We used the best-track dataset from the Joint Typhoon Warning Center (JTWC), which was integrated with the IBTrACS (version 3.10). The data were downloaded from https://www.ncdc.noaa.gov/ibtracs/. The temporal resolution of the data is 6 h.

2.2 *Satellite-based data*

2.2.1 *Sea surface height (SSH)*

Archiving validation and interpretation of satellite data in oceanography (AVISO) was the source of sea surface height gridded data, which are mainly retrieved from TOPEX/Poseidon, Jason 1, ERS-1, and ERS-2 data and merged with ongoing altimeter observations. The AVISO altimeter products were produced and distributed by the copernicus marine and environment monitoring service (CMEMS; http://www.marine.copernicus.eu). The temporal resolution is daily, and the spatial resolution is 0.25°×0.25° (latitude × longitude).

2.2.2 *SST*

We used microwave (MW) and infrared (IR) merged optimum interpolation sea surface temperature (OISST; version 5.0), which is provided by RSS (www.remss.com). The microwave sensors include TMI, AMSR-E, AMSR-2, WindSat, and GMI, and the infrared sensors are moderate resolution imaging spectrora-

diometer-Terra (MODIS-Terra), MODIS-Aqua, and visible infrared imaging radiometer suite-national polar-orbiting partnership (VIIRS-NPP). The temporal resolution is daily, and the horizontal resolutions are 9 km, roughly (1/12)°.

2.2.3 *Surface wind*

The wind products used in this study are from the cross-calibrated multi-platform (CCMP) project (version 2, www.remss.com). CCMP wind vectors were merged with radiometer wind speeds (including SSM/I, special sensor microwave imager/sounder (SSMIS), AMSR, TMI, WindSat, and GMI), scatterometer wind vectors (QuikSCAT and ASCAT), moored buoy wind data, and European Centre for Medium-Range Weather Forecasts (ECMWF) ERA-Interim reanalysis wind fields. The temporal resolution is 6 h, and the horizontal resolution is 0.25°× 0.25° (latitude × longitude).

2.2.4 *Precipitation*

The precipitation data we used are the output of the TMI (www.remss.com), with spatial and temporal resolutions of 0.25°×0.25° (latitude × longitude) and 3 h, respectively.

2.3 *In situ observation*

2.3.1 *Surface drifter*

The surface velocity program (SVP) drifters were used to extract the surface current and *in situ* SST. The drogue depth of SVP drifters is 15 m and the temporal resolution is 6 h. The data were provided by Atlantic Oceanographic and Meteorological Laboratory Drifter Data Assembly Center (AOML DAC) (https://www.aoml.noaa.gov/).

2.3.2 *Argo float*

Argo floats perform profiling measurements on ocean temperature and salinity and therefore provide near-real-time vertical observations of water columns. Argo floats have diverse producers, sampling rates, and parking depths. For a typical Argo float, the water depth is limited to 2 000 m, and the temporal resolution is roughly 1 d to 10 d. The Argo data are available at Global Data Assembly Centre (Argo GDAC) (ftp://ftp.ifremer.fr/ifremer/argo).

2.4 *Analysis and reanalysis data*

2.4.1 *NCEP/NCAR*

The National Centers for Environmental Prediction-National Center for Atmospheric Research (NCEP/NCAR, also known as NCEP-1) atmospheric reanalysis is a relatively old product (Kalnay et al., 1996), and it has relatively coarse grids. The horizontal resolution is about 210 km (T62), and the vertical grid includes 24 levels. According to Kalnay et al. (1996), the assimilated data include rawinsondes, comprehensive ocean-atmosphere data set (COADS) marine surface, aircraft, surface land synoptic data, satellite sounder data, satellite surface wind speeds, and satellite cloud drift winds. The output has a temporal resolution of 6 h and a horizontal resolution of 2.5°×2.5° (latitude × longitude). The data are available at https://www.esrl.noaa.gov/psd/data/gridded/data.ncep.reanalysis.html.

2.4.2 *NCEP-FNL (NCEP final analysis)*

NCEP-FNL is an atmospheric analysis dataset, which uses the most complete set of observations and is run last in the sequence of operational global models. The FNL is likely the best option for a long-term operational model archive from NCEP (Chang and He, 2011). The observations in NCEP-FNL include surface observations, balloon data, wind profiler data, aircraft reports, buoy observations, radar observations, and satellite observations. The NCEP-FNL output has a horizontal resolution of 1.0°×1.0° (latitude× longitude), and the temporal resolution is 6 h.

2.4.3 *ERA-Interim*

ERA-Interim is a global atmospheric reanalysis from the European Centre for Medium-Range Weather Forecasts (ECMWF) (https://www.ecmwf.int/en/forecasts/datasets/reanalysis-datasets/ERA-Interim). The atmospheric model has a horizontal resolution of approximately 79 km (T213) and 60 layers in the sigma-pressure vertical coordinate. ERA-Interim assimilates observations from satellites, aircraft, radiosondes, ocean buoys, and other surface platforms (Uppala et al., 2005; Dee et al., 2011). Specifically, the advantage of its assimilation method is derived from the use of four-dimensional variational assimilation (4DVar) rather than three-dimensional variational assimilation (3DVar), and the numerical model is a coupled atmosphere-wave model. We downloaded the data output with a horizontal resolution of 0.25°×0.25° (latitude×longitude) and a temporal resolution of 6 h.

2.4.4 *HYCOM*

The HYCOM ocean reanalysis combines a hybrid-grid ocean model with operational ocean observations (Cummings, 2005; Cummings and Smedstad, 2013) that cover multi-platform SST (satellite infrared and microwave SST, surface platform SST, CMAN SST, etc.), altimeter SSH, sea ice concentration, and ocean profiling data (XBT, Argo floats, CTD stations, drifting buoys, and fixed buoys). The data are available at http://ncss.hycom.org/thredds/ncss/grid/GLBu0.08/expt_91.2/dataset.html, with 0.08°×0.08° (latitude × longitude) horizontal resolution and daily temporal frequency.

3 Results

3.1 *Super typhoon Meranti*

Super typhoon Meranti originated as a tropical depression on the night of 8 September 2016 near Guam (Fig. 1). It moved northwestward and developed into a tropical storm on 10 September. There are a number of mesoscale eddies in this specified regions. During the generation and development of Meranti, a weak cold eddy was identified at 18°N, 130°E. Meanwhile, a strong warm eddy was located in the east of the Luzon Strait, centered at 20°N, 125°E. Both the cold and warm eddies were pre-existing in the track of Meranti. Starting from 06:00 UTC on 11 September, it quickly strength from Category 1 to Category 5 according to the Saffir-Simpson scale. From 12:00 UTC on 12 September, when Meranti began to passed through the warm eddy, it immediately reached up Category 5, to 00:00 UTC on 14 September, Category 5 stage persisted for about 36 h. On the morning of 14 September, Meranti quickly weakened and then landed at Fujian Province, China.

According to the change of sea level anomaly (SLA), we can expect that typhoon has a probability to strengthen the weak cold eddy and weaken the warm eddy, since the maximum decrease of SLA appeared in the weak cold eddy (–20 cm) after the passage of Meranti, while the decrease of SLA in the warm eddy was much smaller (–10 cm, figure not given here).

In the time series of best-track data from JTWC (Fig. 2), the concave shape of central pressure (P_c) indicates the continuous

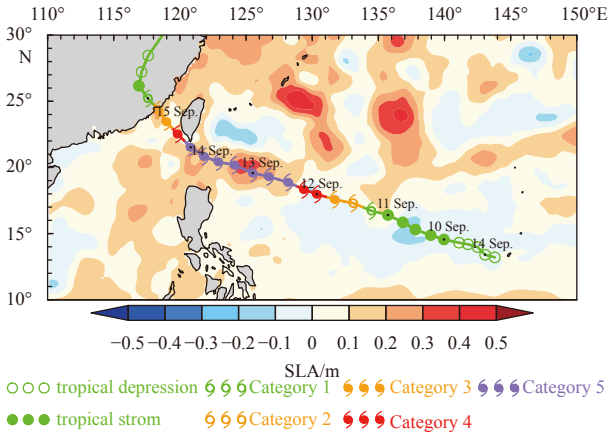

Fig. 1. Track and intensity of super typhoon Meranti in September 2016. The marked black dots indicate 00:00 UTC of everyday. The color shading indicates the 3 d averaged (10–12 September) SLA from AVISO before Meranti reached the category of super typhoon.

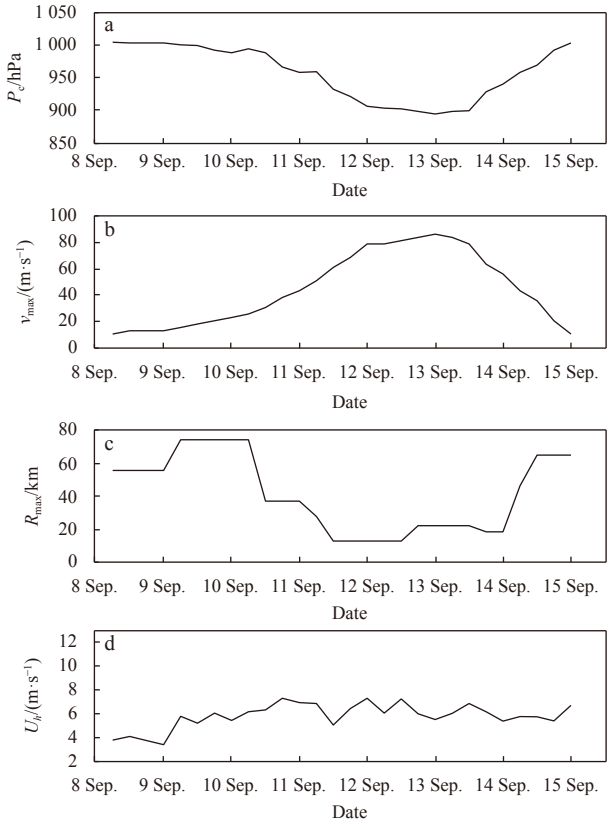

Fig. 2. Time series of central pressure (P_c), maximum sustained wind (v_{max}), radius of maximum sustained wind (R_{max}), and translation speed (U_h) of super typhoon Meranti. The light grey and dark grey area represent the stage of Category 4 and Category 5, respectively.

enhancement of the central eye, and the minimum pressure was 890 hPa. At the Category 5 stage, the maximum sustained wind speed (v_{max}) was more than 80 m/s and the radius of the maximum sustained wind (R_{max}) was less than 18 km. It is noted that the small R_{max} value requires considerable horizontal resolution to resolve the typhoon core structure. Meranti moved relatively slowly (4–6 m/s) during the early stage, and after 11 September, Meranti moved relatively faster and attained a translation speed (U_h) of roughly 6.5 m/s. The evolution of maximum wind stress or air-sea momentum flux was similar to that of v_{max}, reaching a peak of 13.0 N/m^2 (Appendix A).

3.2 *SST*

Figure 3 shows the evolution of SST; the left panels are snapshots of SST, and the right panels are the SST variation referenced to 00:00 UTC on 9 September (Fig. 3a). The red lines show the best-track, while the green and black contours represent –1.0°C and –1.5°C cooling patches. At the beginning of Meranti, the WNP was covered by warm waters, and SST reached a high value of 31°C (Fig. 3a). Footprint of Meranti is revealed as SST cools along the best-track.

At 12:00 UTC, 11 September (Fig. 3c), the first cooling patch appeared, which was closely associated with the weak cold eddy in Fig. 1. The second large cooling core appeared in the southeast of the pre-existing warm eddy after 48 h. This time, the decrease in SST was more than 2.0°C, while the first cooling patch continued to enlarge (Fig. 3e). The pattern of SST cooling displays clear right-bias distribution. Later, as shown in the snapshot of 12:00 UTC on 15 September (Fig. 3g), the spatial coverage of the 1.5°C decrease in SST was about 4°×3° in zonal and meridional directions, respectively. Meanwhile, the 1.0°C SST cooling area expanded to 8°×5° in the zonal and meridional directions, respectively. This cooling pattern lasted for a few days after Meranti landed.

Figure 4 shows the variation in SST during Meranti in the reanalysis data. For NCEP/NCAR (Figs 4a and b), the SST snapshot at 12:00 UTC on 9 September represents the initial state before the typhoon arrived. It looks relatively smooth and is missing high-wavenumber variances because of the coarse grid. NCEP/NCAR reanalysis SST data lack the typical ocean dynamics since the SST cooling appears to be very weak, with the 0.5°C cooling area nearly absent from the sea surface. National Centers for Environmental Prediction-final analysis (NCEP-FNL) resembles the MW_IR OISST pattern (Fig. 4c), however, Fig. 4d shows that the SST cooling was distributed around but not under the typhoon track. Compared with MW_IR OISST, SST cooling is weaker in this dataset: The 1.0°C cooling area is very small and in a location that differs from that specified by MW_IR OISST. Meanwhile, SST cooling does not have the right-side bias that appears in the MW_IR OISST field. The initial SST from ERA-Interim (Fig. 4e) is similar to that from MW_IR OISST (Fig. 3a), but the subsequent SST cooling (Fig. 4f) does not appear to be as strong as that indicated by MW_IR OISST. As the sole oceanic reanalysis in the present study, HYCOM better characterizes SST cooling (Figs 4g and h). SST cooling occurred along the typhoon track, and the location is in the east of the Luzon Strait. Nevertheless, HYCOM overestimates SST cooling: It presents the 1.0°C cooling as 10°×6° in the zonal and meridional directions, and the cooling area is larger than that in MW_IR OISST.

3.3 *Surface wind*

We rebuilt the wind field using best-track data and an idealized wind structure (Holland, 1980; Yablonsky and Ginis, 2009, Appendix B). Figure 5 shows the rebuilt wind data compared with CCMP data. When Meranti reached super typhoon intensity, R_{max} was about 18 km (Fig. 2). The idealized wind field is able to describe the core structure because of the high horizontal grid

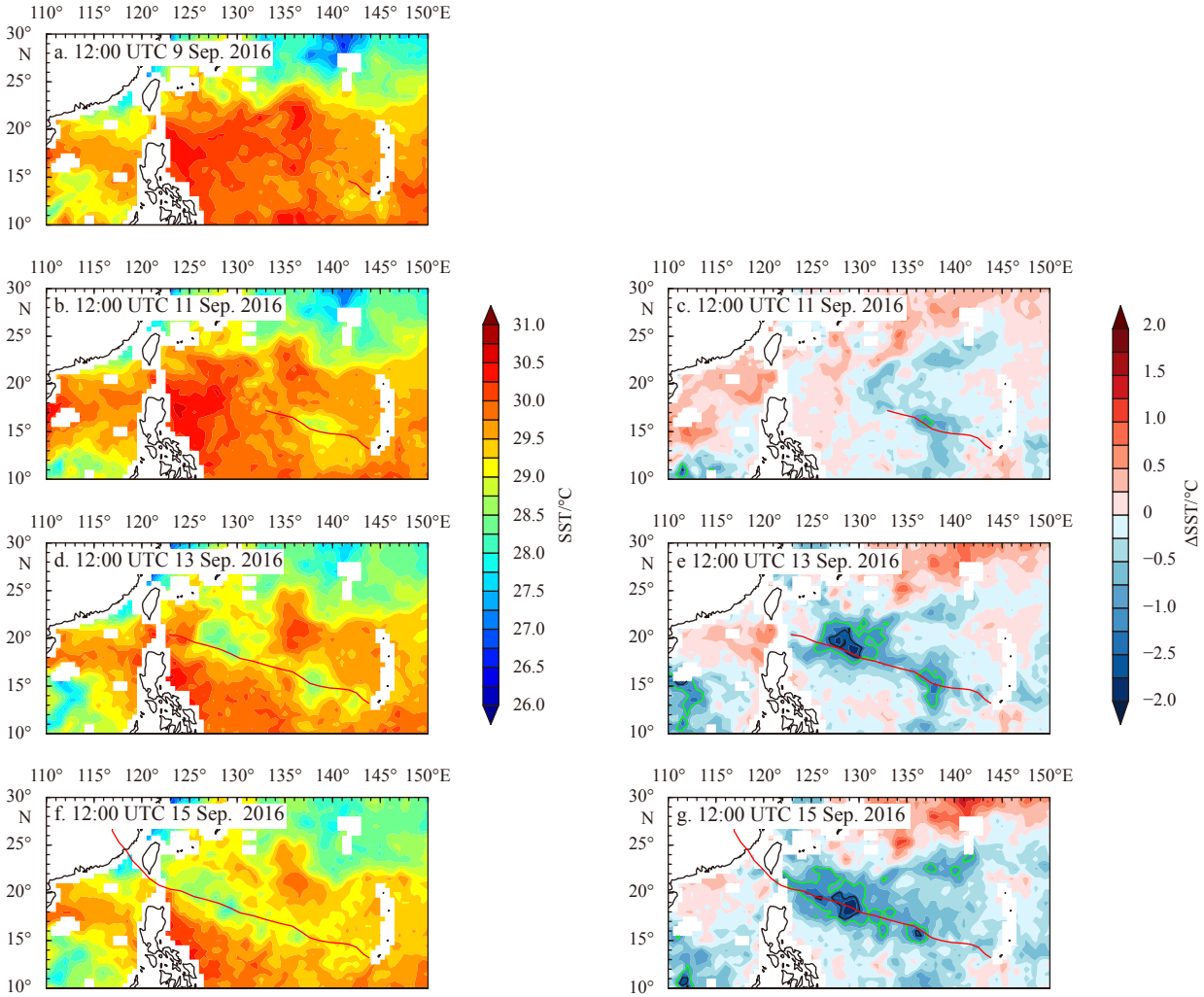

Fig. 3. Evolution of SST during super typhoon Meranti (2016) from MW_IR OISST; the left panels (a, b, d, f) are snapshots of SST, and the right panels (c, e, g) are the SST variation referenced to (a). The red lines are the best-track, and the green and black contours represent –1.0°C and –1.5°C cooling patches. For better visualization, we plotted the data in 0.5°×0.5° grids.

resolution (0.125°×0.125°). In contrast, the horizontal resolution of the satellite data (CCMP) is relatively coarse (0.25°×0.25°). As a result, the CCMP data cannot depict the details of the core structure. CCMP wind data also indicates that Meranti had an asymmetric structure, with the snapshots revealing that the wind was right-side biased. Also, compared with the coverage of Meranti as portrayed by the idealized wind field, CCMP suggests broader coverage; at super typhoon stage, this discrepancy is associated with the different shape coefficient in the idealized wind field.

Figure 6 depicts the evolution of surface wind according to NCEP/NCAR, NCEP-FNL, and ERA-Interim. The wind, according to NCEP/NCAR, was relatively weak. The horizontal structure described by the NCEP-FNL wind data is more consistent with that derived from satellite observations, and NCEP-FNL wind data are characterized by a mainly symmetric distribution (Fig. 5). A noteworthy difference between NCEP-FNL and the idealized wind vortex is that the NCEP-FNL-based radius of the typhoon core is larger at the super typhoon stage (approaching and crossing the Luzon Strait). The surface wind from ERA-Interim is very close to that from CCMP (Fig. 5). The distribution of the ERA-Interim reanalysis wind data is concentrated on the right side and decreases on the left side (as shown in Fig. 6). This pattern clearly resembles that derived from the satellite product.

3.4 *Precipitation*

Figure 7 shows the precipitation during typhoon Meranti. We can easily capture the typhoon-induced extra precipitation along the track and see that it increased on the left side of the typhoon track. There was additional precipitation on the eastern coastline of Taiwan and Fujian, and the maximum accumulated precipitation occurred around Taiwan Island (about 23°N, 121°E).

During the generation period of Meranti, the precipitation rate was relatively high at 25 mm/h with an asymmetric distribution (Fig. 7a). From 11 September to 12 September, the precipitation rate decreased to 16 mm/h but with a vortex distribution. From 12:00 to 18:00 UTC on 13 September, the precipitation rate quickly increased from 20.0 mm/h to 32.5 mm/h (Fig. 7e), which was probably related to the oceanic warm eddy just below the typhoon. As Meranti landed on the southeast coastline of China, both the rate and coverage of heavy precipitation gradually decreased. Figures 7b–h show the accumulated precipitation from 18:00 UTC on 11 September to 18:00 UTC on 14 September. Enhanced precipitation was pronounced along the typhoon track and was left-biased. The accumulated precipitation during Mer-

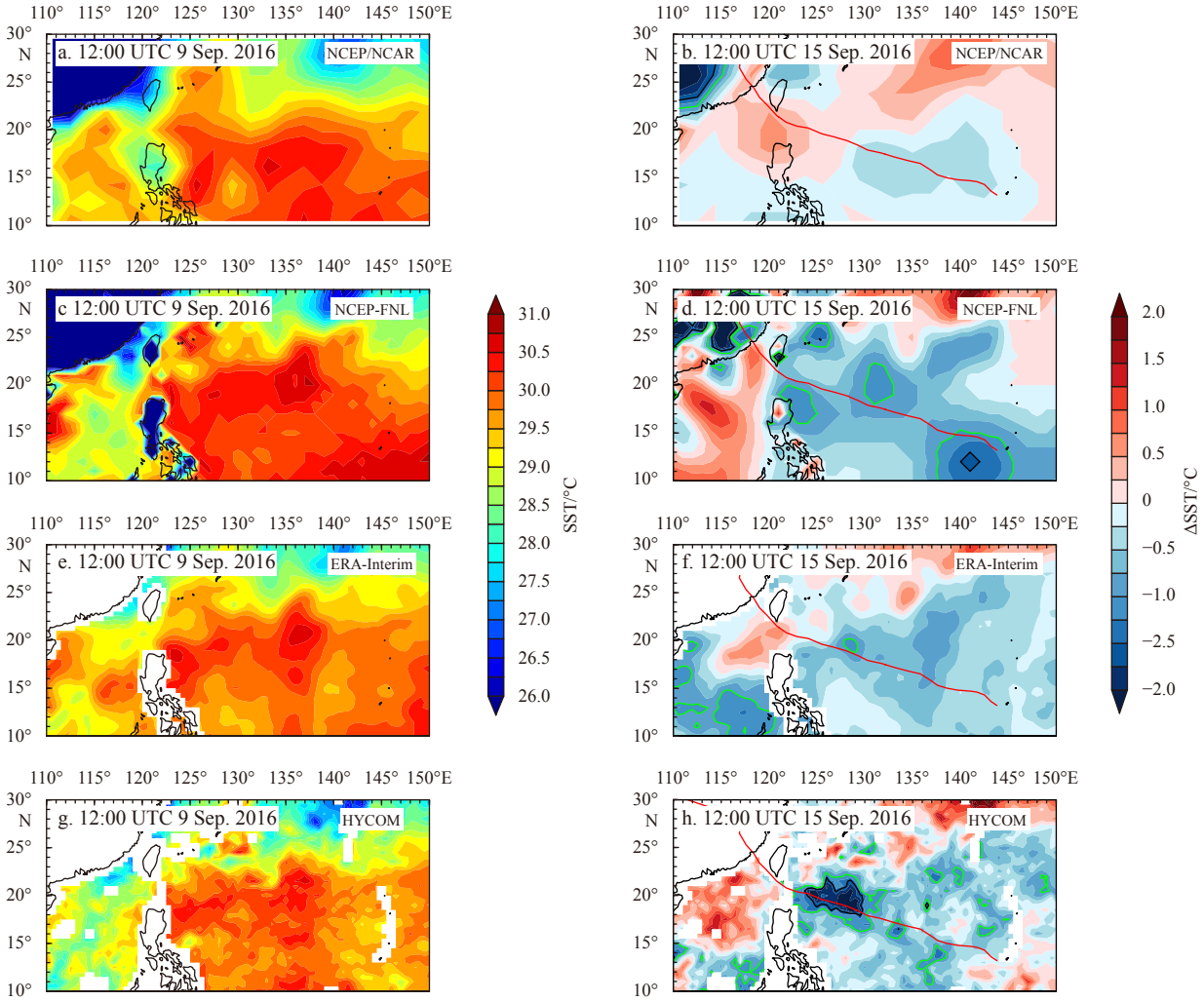

Fig. 4. Evolution of SST from (a, b) NCEP/NCAR, (c, d) NCEP-FNL, (e, f) ERA-Interim, and (g, h) HYCOM during super typhoon Meranti. The left panels (a, c, e, g) are the SST at the initial time, and the right panels (b, d, f, h) are the SST changes relative to the left panels after the landing of Meranti. The red lines are the best-track, and the green and black contours represent –1.0°C and –1.5°C cooling patches.

anti reached 320 mm. Another high precipitation system appeared around 13°N, 140°E, and the accumulated precipitation was larger than 340 mm (Fig. 7f). This heavy rain was probably caused by the sequential typhoon Malakas, which was generated around 11°N, 145°E at 18:00 UTC on 11 September (Fig. 7c). Meanwhile, from the satellite-derived data, we found a heavy cloud coverage happened in the same location, since this area is close to the generation position of typhoon in WNP, we believe this heavy rain has a relationship with the cloud cover above.

3.5 *Surface drifter*

Figure 8a depicts the trajectories of the surface drifters. Four drifters (identified as 133223, 127307, 127384, and 127257) were coincidentally close to the track of Meranti. The red dots in Fig. 8 indicate the positions of the drifters when Meranti originated, and the red crosses indicate the position of the drifters when Meranti arrived. Here, we define the arrival time of the typhoon as the time at which the distance between the typhoon center and the drifter (or Argo float in next subsection) was at its minimum distance. The trajectories of the left-side drifters (127307 and 127384) continued to move westward. For the right-side drifters, 133223 first moved in the southwest direction toward the typhoon track during the typhoon, then, it moved in the northwest direction after it passed by the typhoon. Drifter 127257 first moved eastward and circularly westward in a relatively big loop, which reflects the influence of the warm core eddy in the area (Fig. 1). After the passage of Meranti, the movement of drifter 127257 was confined to small circles around a specific point (Fig. 8a).

From the variation in SST (blue lines in Figs 8b–e), we can observe that before the arrival of Meranti, the SST of the four drifters maintained an oscillating upward trend. Close to the typhoon arrival time, SST rapidly dropped by 1°C. Two days before the typhoon arrived, the left-side drifters 127307 and 127384 were about 31.0°C. Their SST then dropped to 30.0°C upon the arrival of the typhoon and further dropped to 29.9°C and 29.7°C, respectively. For the right-side drifter 133223, SST dropped from 30.7°C to 29.6°C, while SST of drifter 127257 dropped from 30.3°C to 29.0°C.

The time series of near-surface current shows that the left-side drifters (127307 and 127384) were limited to zonal current before the typhoon arrived (consistent with the trajectory), and

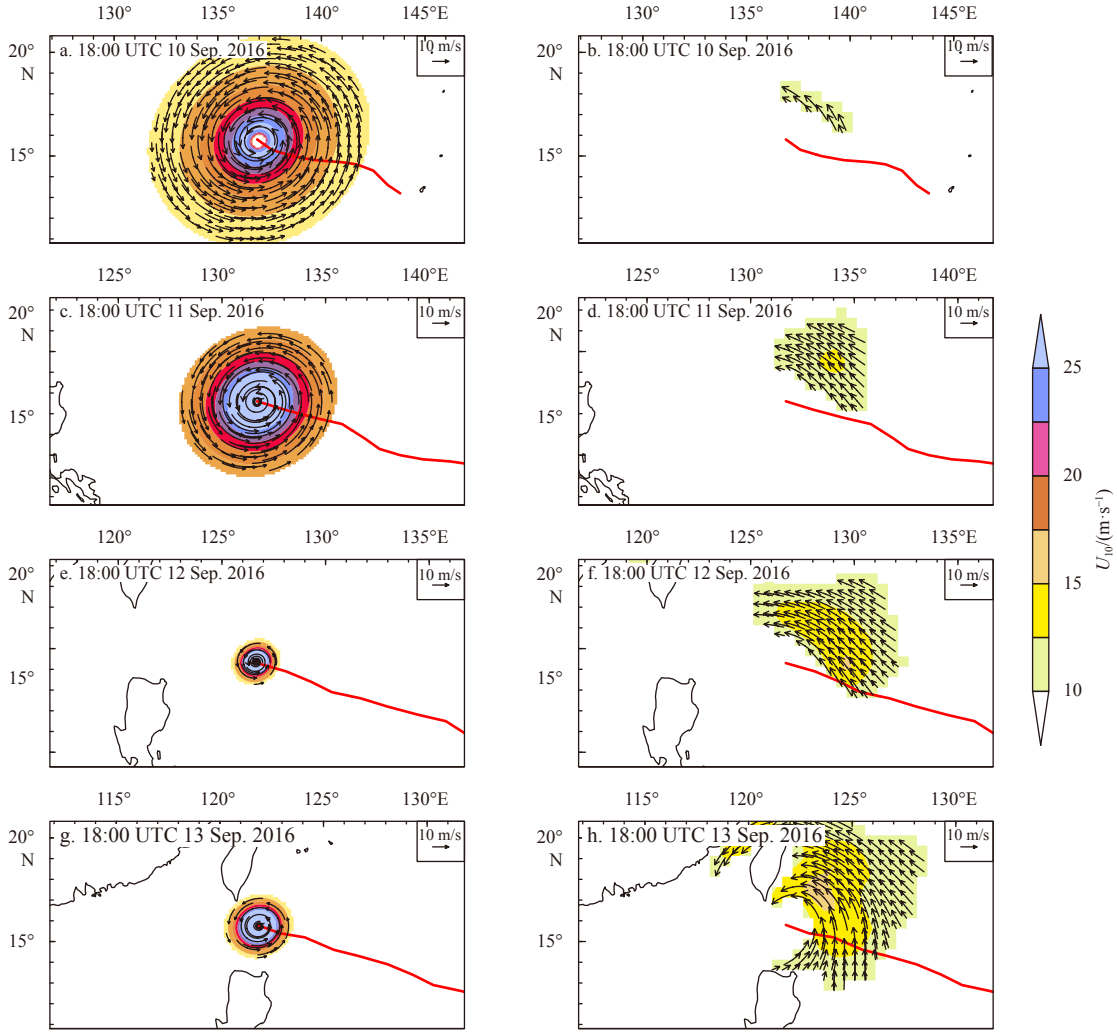

Fig. 5. Wind field of super typhoon Meranti. The left panels (a, c, e, g) are constructed from the idealized wind vortex, and the right panels (b, d, f, h) depict satellite-based CCMP data. The red lines represent the best-track of Meranti. The shaded areas represent the wind speed at 10 m (U_{10}) above the sea surface.

slightly weak oscillations were stimulated by the typhoon. Near-inertial oscillations for the right-side drifters (133223 and 127257) were evident after the typhoon passed. For 127257, the transient *u* current attained a magnitude of 2.0 m/s.

3.6 *Argo float*

The observational locations of the Argo floats in September 2016 are shown in Fig. 9a. Three floats (black lines; IDs of 2902666, 2901543, and 2902953) are shown that were near the TC track and had suitable sampling frequencies. The red points indicate the location of the first profile in September, while the red crosses indicate the location of the profile at the arrival time of Meranti (t_0). From the trajectories in Fig. 9a, floats 2902666 and 2901543 drifted a considerable distance in September, while float 2902953 was apparently trapped around 20.5°N, 129.5°E. It is also noted that float 2901543 moved from the left side to the right side of the TC track, while float 2902666 moved roughly parallel to the track.

The variations in temperature and salinity profiles in the uppermost 300 m are shown in Figs 9b–g. Float 2902666 recorded a clear near-surface cold wake after the typhoon passed. At the same time, the subsurface was substantially warmed as a result of vertical mixing between the near-surface water and subsurface water. The SST cooling was about 1.0°C after 0.4 d of the typhoon passing, and the mixed-layer depth increased 30 m (mixed-layer depth is defined as the depth where the density is 0.25×10^{-3} kg/m^3 higher than that at the surface; Fig. 9b). A salinity response to the typhoon is also evident in Fig. 9e. At 1.4 d before the typhoon arrival t_0, the freshwater level near the surface and the salinity sharply increased from 34.50 to 34.70 in the uppermost 20 m, and then the salinity gradually increased to 35.10 at 180 m. Later, during the typhoon forcing period (t_0+0.4 d), the sharp near-surface salinity gradient disappeared. The salinity above 90 m was almost the same, which represents the base of the mixed layer from the temperature profiles. The large vertical temperature and salinity gradients between 90 m and 120 m imply that there was strong stratification between the warm-fresh water in the uppermost layer and the cold-saline water in the lower layer. Subsequently, the strong stratification layer was shifted downward at t_0+2.3 d and shifted upward at t_0+3.1 d. These observations are indicative of the relatively intense oscillation of the thermocline.

The minimum distance between float 2901543 and the typhoon center was 53 km, which is comparable to the radius of the maximum wind. The wind oriented toward the inner low-pressure center probably led to the float drifting from south to

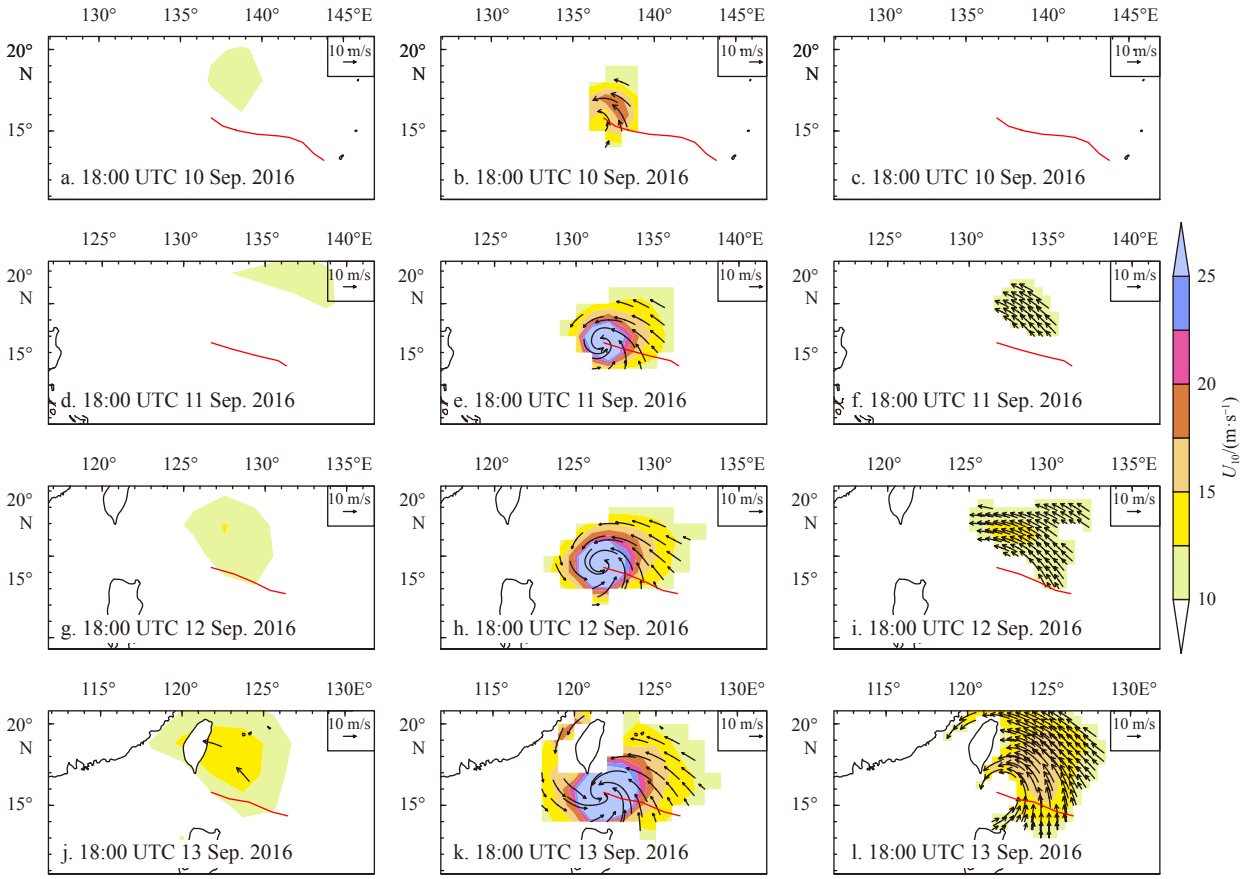

Fig. 6. Surface wind from NCEP/NCAR (a, d, g, j), NCEP-FNL (b, e, h, k), and ERA-Interim reanalysis (c, f, i, l). The shaded areas represent the wind speed at 10 m (U_{10}) above the sea surface. The red lines represent the best-track of Meranti.

north. On the other hand, float 2901543 was just below the typhoon center when the typhoon passed. Here, as a typical ocean response to a typhoon, an upwelling signal is identifiable in Fig. 9c. Comparing the two profiles at –1.3 d and 0.5 d reveals that the temperature in the uppermost 50 m was not markedly decreasing; however, the thermocline was uplifted by 30 m. The 28°C depth was 100 m just prior to the typhoon arrival and 70 m just after the typhoon arrival. The upwelling signal is also evident in the salinity profiles in Fig. 9f. The halocline at a depth of 90 m was uplifted to 60 m between –1.3 d and 0.5 d relative to the typhoon arrival time, and the corresponding gradient was further enhanced at the base of the mixed layer.

The signals induced by Meranti were relatively weak but still identifiable from float 2902953. In Fig. 9d, the temperature profile just before the typhoon arrived shows a relatively shallow mixed layer (about 30 m), and the temperature in the mixed layer was 30.0°C. After the typhoon passed, the mixed-layer depth shifted downward to 50 m, and the temperature decreased to 29.5°C. In particular, the subsurface layer of water between 80 m and 250 m was significantly warmed up. The salinity change after the typhoon was much saltier in the uppermost 40 m, slightly fresher between 40–90 m, and saltier between 90 m and 250 m (Fig. 9g).

3.7 *Comparisons among multi-platform datasets*

3.7.1 *Comparisons of SSTs between satellite and in situ observations*

We compared the SST between *in situ* observations from ocean measurements and multi-satellite products, as shown in Fig. 10. Considering the *in situ* data from SVP drifters and Argo floats are more reliable, we interpolated the daily MW_IR OISST into the drifter/float coordinates, and obtained the drifter/float-following time series. For SVP drifters (Figs 10a–d), the SSTs at 2 d prior to typhoon arrival time were underestimated by satellite product. In SVP 127307 (Fig. 10a), the SST of SVP drifter was 30.5°C at 12:00 UTC 10 September (2 d before TC arrival time), while the SST of MW_IR was 30.0°C. Similarly, there was roughly 0.3°C bias for satellite SSTs at 2 d before typhoon arrival in SVP 133223, 127384, and 127257. Otherwise, the systematic bias was not observed at the typhoon arrival time. The corresponding SVP SSTs were consistent with satellite SSTs for SVP 127307 and 133223, while the SVP SST was higher (lower) than MW_IR SST for SVP 127384 (127257). Furthermore, for the intensity of SST cooling, the *in situ* SST differences between 2 d before and after typhoon arrival times were –0.5°C, –0.6°C, –0.8°C and –0.9°C for SVP 127307, 133223, 127384 and 127257, respectively. The corresponding SST cooling of satellite data was –0.7°C (SVP 127307), –0.2°C (SVP 133223), –0.9°C (SVP 127384) and –0.8°C (SVP 127257), respectively. Therefore, the MW_IR SST cooling was close to the *in situ* observation in most SVP drifters (SVP 127307, 127384, and 127257).

For the Argo floats (Figs 10e and f), the sampling rate was considerably lower than SVP drifters. Nonetheless, two aspects are observed as similar to SVP drifters. First, the satellite product preferred to underestimate the SST at 2 d before TC arrival time. Second, the SST cooling intensity was nearly same between Argo

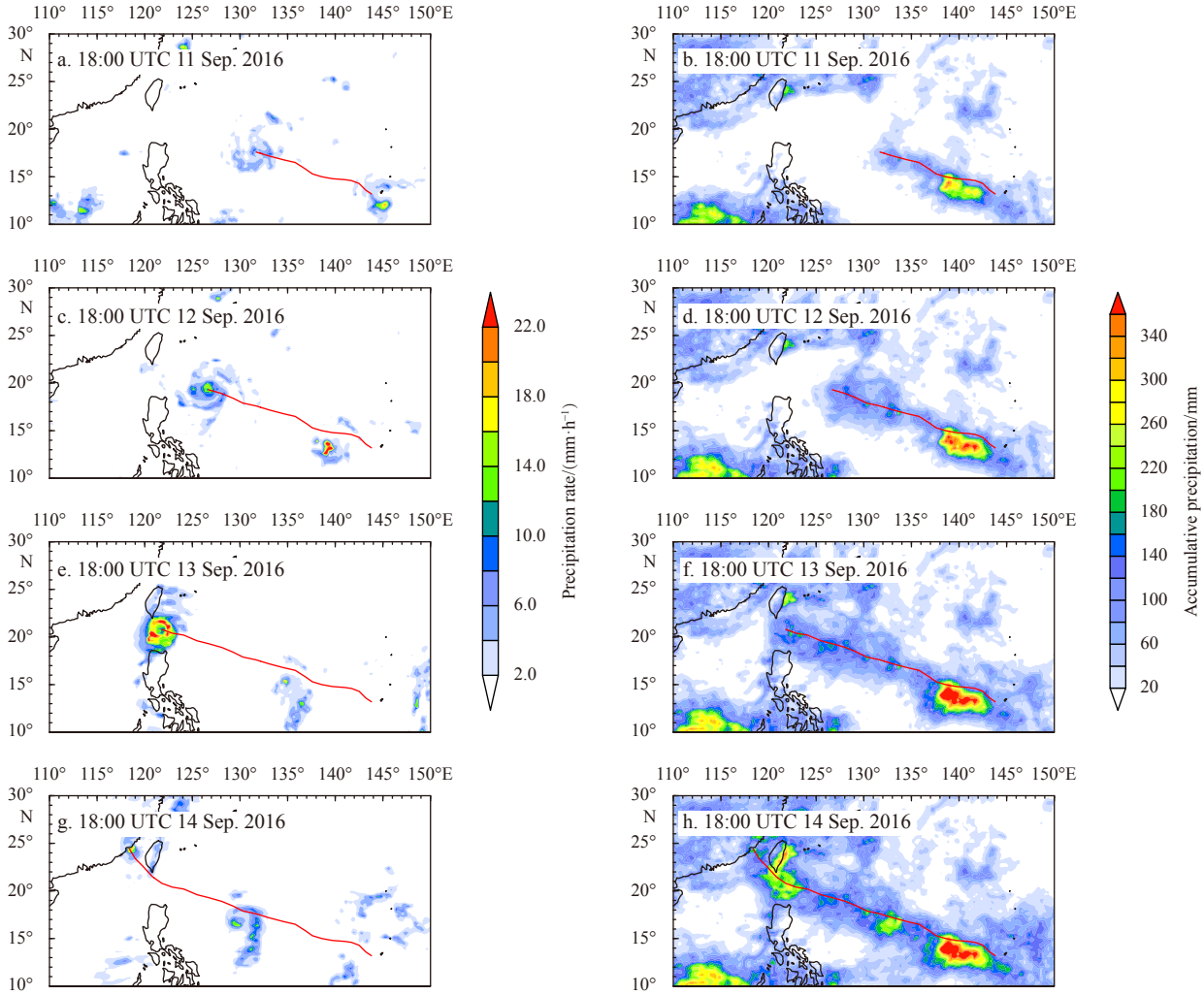

Fig. 7. Snapshot precipitation (a, c, e, g) and accumulative precipitation (b, d, f, h) from the TMI during the period of Meranti. The red line shows the evolution of the typhoon center.

float and satellite product.

3.7.2 *Correlation between sea surface salinity and precipitation*

Strong anomaly precipitation during typhoon bring extra freshwater to sea surface, and presumably reduces the sea surface salinity (SSS). Figure 11 show the time series of SSS from Argo floats and the precipitation rate from TMI. It is observed, as in the Argo-following record, the heavy precipitation occurred at the typhoon arrival time. The transient precipitation rate attained roughly 8.0 mm/h in Argo 2902666 and 2901543. However, the SSSs in Argo floats were not significantly reduced due to the precipitations. In contrast, the SSS increased 0.10 at typhoon arrival time in Argo 2902666 (Fig. 11a). According to the corresponding profiling analysis (Fig. 9e), at the time of 1.4 d before typhoon arrival time, a thin fresh water layer was formed at the near surface. Later, at the forcing period of typhoon (0.4 d after typhoon arrival time), the former near-surface thin fresh water layer was destroyed by the vertical mixing, and the near-surface salinity increased and the corresponding deeper water decreased. Similarly, the SSS of Argo 2901543 slightly increased after typhoon pass-by (Fig. 11b). It is worthy to mention that Argo 2902666 did a relatively longer excursion, and Argo 2901543 stayed at a relatively fixed-position (Fig. 9a), therefore Argo 2901543 was more likely to be a fixed-position observation. Hence, the SSS response here is more likely contributed by the upper ocean vertical mixing other than the surface freshwater forcing.

4 Discussion

Three atmospheric analysis/reanalysis including NCEP/NCAR, NCEP-FNL and ERA-Interim all underestimate the typhoon-induced SST cooling. If these atmospheric analysis/reanalysis were used for atmospheric model configuration, the initial SST was warmer than the realistic ocean, and the air-sea sensible and latent heat fluxes would be amplified. Accordingly, the typhoon would gain more heat fluxes from ocean, and therefore the intensity of typhoon would be increased (Cione, 2015; Sun et al., 2019). Meanwhile, the enhanced latent heat flux bought more water vapor from ocean to atmosphere, and changed the vertical structure of the atmospheric moisture (Bao, 2016; Sun et al., 2019). In other word, the initial SST error from atmospheric analysis/reanalysis would impose broadly impacts on the atmospheric model. However, the oceanic reanalysis (HYCOM) gives relative good SST evolution. Some of the differences among these analysis/reanalysis fields are due to the model resolution. Nevertheless, the results imply that the coupled atmo-

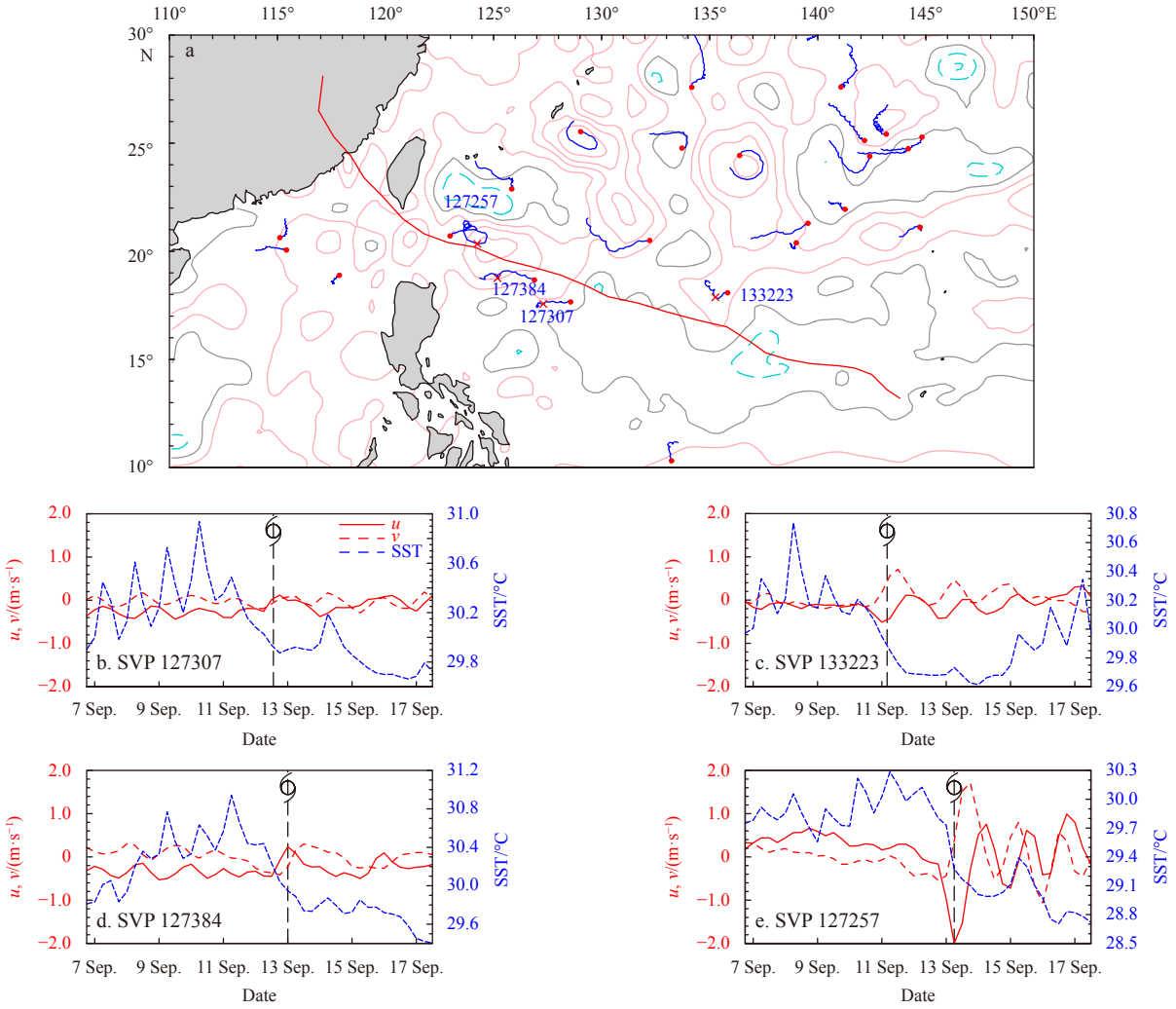

Fig. 8. Trajectories of surface drifters near Meranti (a), and time series of near-surface current and SST (b, c, d, e). In a, the red points indicate the drifter positions when Meranti originated; and the red crosses indicate the drifter positions when Meranti arrived; the background contours are the SLA (solid pink lines for positive values, dashed turquoise lines for negative values, and solid gray lines for zero). In b–e, the black dashed line with the typhoon symbol represents the arrival time of Meranti (t_0).

sphere-ocean model is essentially required for the typhoon forecasting, and the atmosphere-only model is comparably not sufficient in describing the SST cooling as well as the typhoon-ocean interaction.

Meranti achieved super typhoon intensity at WNP, however, the SST cooling induced by typhoon was relatively weak around an anticyclone mesoscale eddy. In the Northern Hemisphere, the anticyclone eddy is most likely warm core eddy. The influences of anticyclone eddy on SST response include two aspects: (1) Anticyclone eddy leads to deeper mixed-layer, and (2) anticyclone eddy promotes the generation of near-inertial internal wave, which brings the mechanic energy of near-surface current downward. Both mechanics cause weaker SST cooling (Lee and Niiler, 1998).

5 Conclusions

The best-track data show that Meranti originated near Guam on 9 September 2016. It then moved northwest to the Luzon Strait and finally landed at Fujian Province, China. The minimum pressure of the typhoon center was 890 hPa, and the corresponding maximum wind speed was more than 80 m/s. The translation speed of Meranti was relatively stable at 6.5 m/s for the period of Categories 4 and 5.

In this paper, we describe the evolution of Meranti in terms of SST, surface wind, and precipitation. The maximum SST cooling induced by Meranti was about 2.0°C, and the cooling mainly occurred on the right-hand side of the typhoon track. The cooling patch is quantitatively defined by 4° in longitude and 3° in latitude for the 1.5°C cooling, and the size expanded to 8° in longitude and 5° in latitude for the 1.0°C cooling. Satellite-based wind data (CCMP) are not sufficient to describe the core structure of the TC because the spatial resolution is relatively low compared with the radius of the maximum wind. However, it is feasible to build an idealized wind vortex to overcome the coarse grids of the satellite data. At the peak of Meranti, the precipitation rate reached 32.5 mm/h and the typhoon eye was clearly captured by the satellite data.

Furthermore, we investigated the ocean response to Meranti using *in situ* data from surface drifters and Argo floats. The observations from the surface drifters reveal that the dynamic response was relatively weak on the left side of the typhoon track and relatively strong on the right side. Accordingly, near-inertial

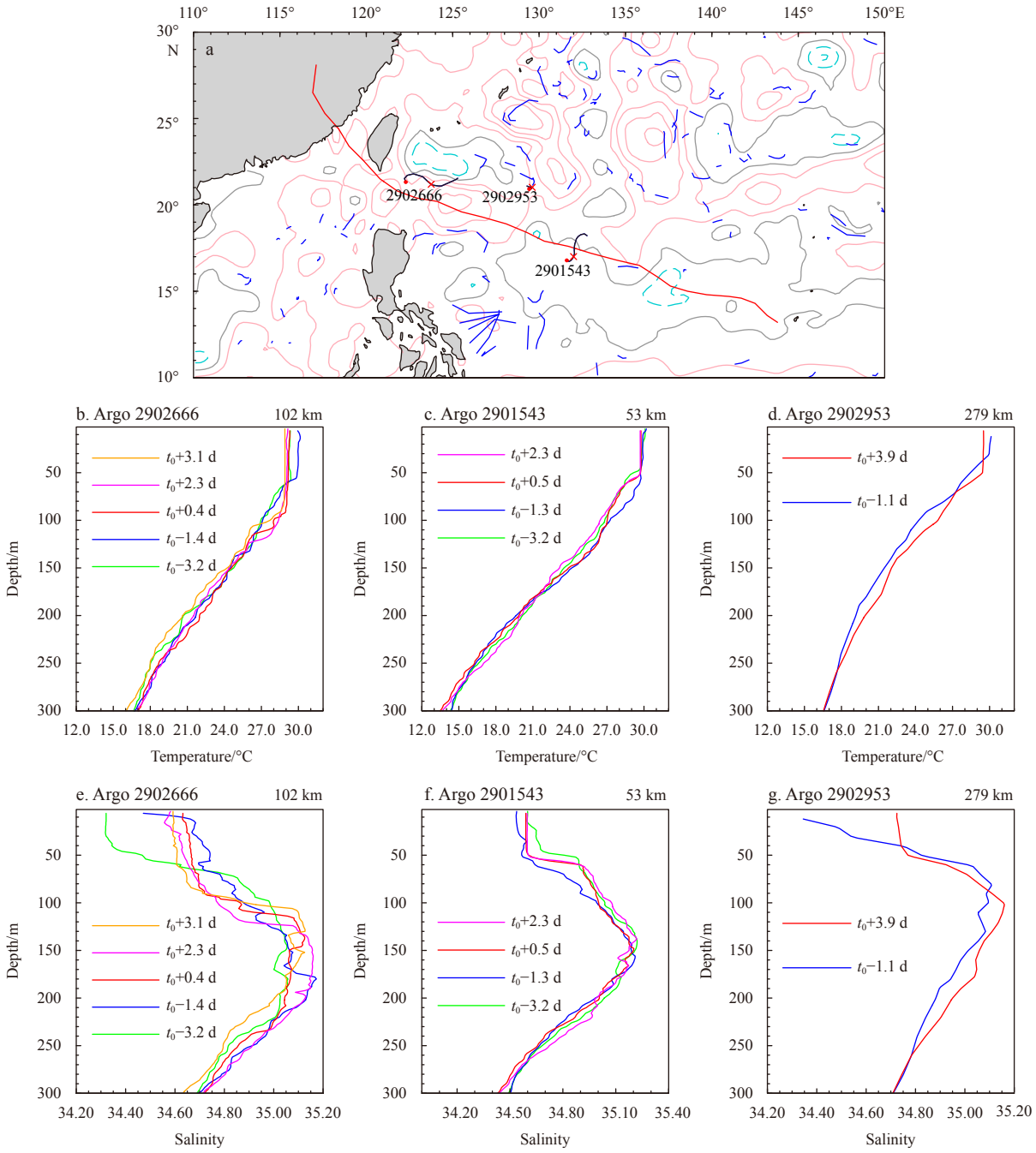

Fig. 9. Trajectories of Argo floats in September 2016 (a, blue and black lines), temperature profiles from Argo floats before and after Meranti (b, c, d), and salinity profiles from Argo floats before and after Meranti (e, f, g). In a, the three black lines are presented for profiling analysis, in which the red points indicate the location of the first profile in September, while the red crosses indicate the location of the profile at the arrival time of Meranti). The background contours are the SLA (solid pink lines for positive values, dashed turquoise lines for negative values, and solid gray lines for zero). In b, c, d, e, f and g, t_0 is the arrival time of typhoon; the minimum distance between the Argo float and the typhoon track is marked in the top-right of subfigures.

currents were observed on the right-side drifters. The SST cooling reached 1.0°C on both the left and right sides of the typhoon track. The limitations imposed by the sparse distribution and long sampling intervals of the Argo floats led to very few floats being located near the passage of Meranti; thus, data from only three floats were used in this study. There was a clear near-surface cold wake captured by float 2902666 after the typhoon passed. Subsurface warming and entrainment of the mixed layer were detected in the vertical temperature and salinity profiles. The SST cooling was about 1.0°C after 0.4 d of the typhoon passing, and the mixed-layer depth extension was about 30 m. The mixed-layer salinity decreased by an average of 0.1. After the typhoon passage, a large vertical gradient of temperature and salinity between 90 m and 120 m was formed, which implies strong stratification between the warm-fresh water in the uppermost layer and the cold-saline water in the lower layer.

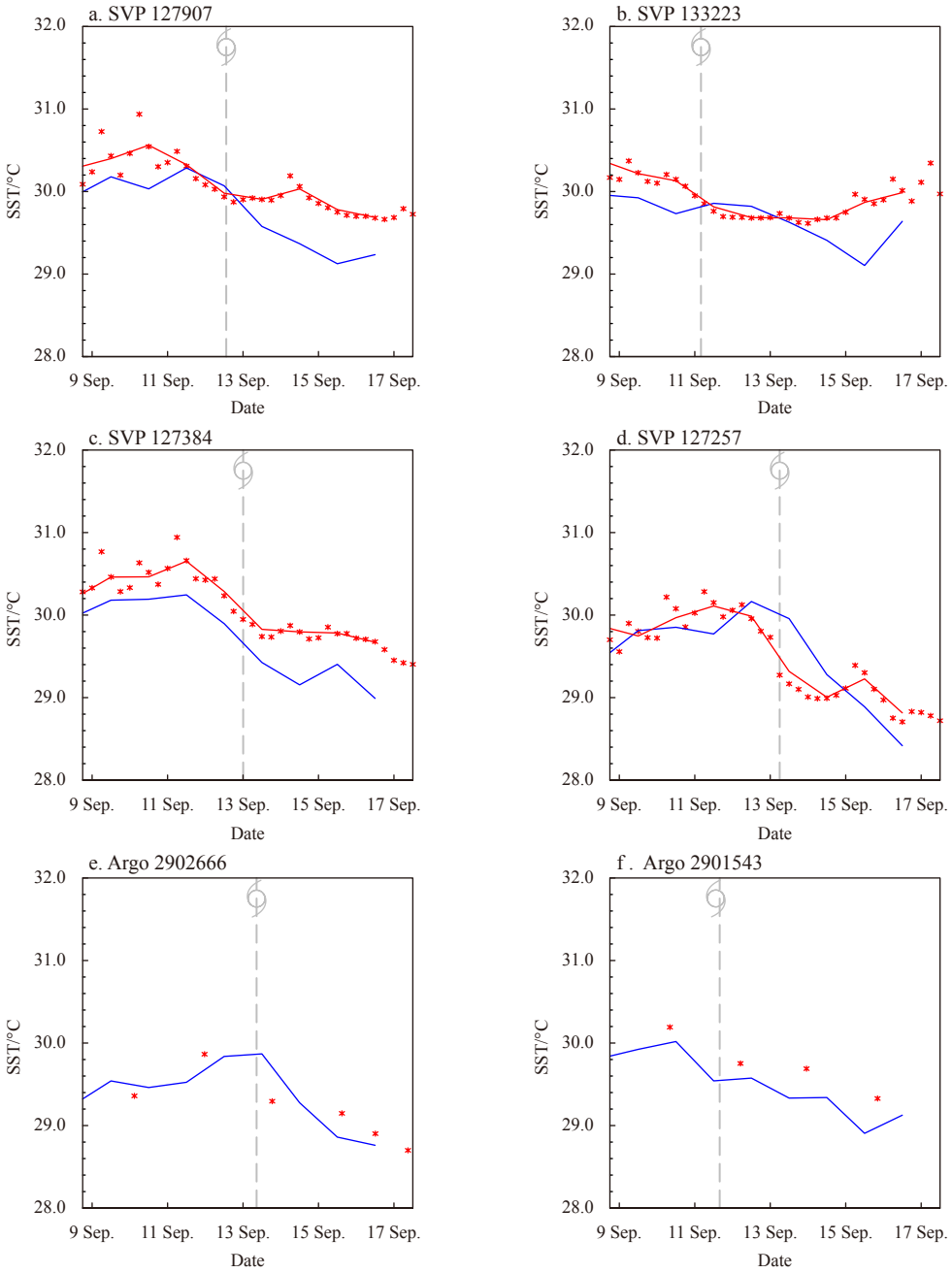

Fig. 10. Comparisons of SSTs between satellite products and *in situ* observations. Blue lines stand for the result from MW_IR OISST. a–d for SVP drifters (red asterisks are the SVP records with 6 h interval, and the red lines are the corresponding daily mean), and e–f for Argo floats (red asterisks).

As a common feature, atmospheric reanalysis underestimates the typhoon-induced SST cooling. The intensities of SST cooling during Meranti according to NCEP/NCAR, NCEP-FNL, and ERA-Interim data are all lower than that from the satellite data. From NCEP/NCAR data, SST cooling is barely detectable and accompanied by relatively weak wind. From NCEP-FNL data, the underestimated SST cooling potentially contributes to the relatively broad eye structure. From ERA-Interim, the SST cooling pattern resembles that from the satellite product, but it is considerably weak. HYCOM reproduces but overshoots the SST cooling that was induced by Meranti. Therefore, to perform hindcast experiments on Meranti, we can conclude from the results of this study that the most reasonable SST forcing data are from the satellite product for both the initial conditions and the variation induced by oceanic dynamics (SST cooling).

Regarding the data quality of satellite SST, the comparisons of SST between satellite and in situ oceanic observations reveal two aspects. First, MW_IR OISST underestimated initial SST at time of 2 d prior to typhoon arrival, and the bias was approximately 0.3°C. Second, MW_IR OISST roughly kept consistent with drifter/float on typhoon-induced SST cooling. Therefore, the results suggest to correct a system bias of MW_IR OISST before use as initial and boundary conditions in atmospheric and oceanic models.

As far as the SSS were concerned, the records in Argo floats

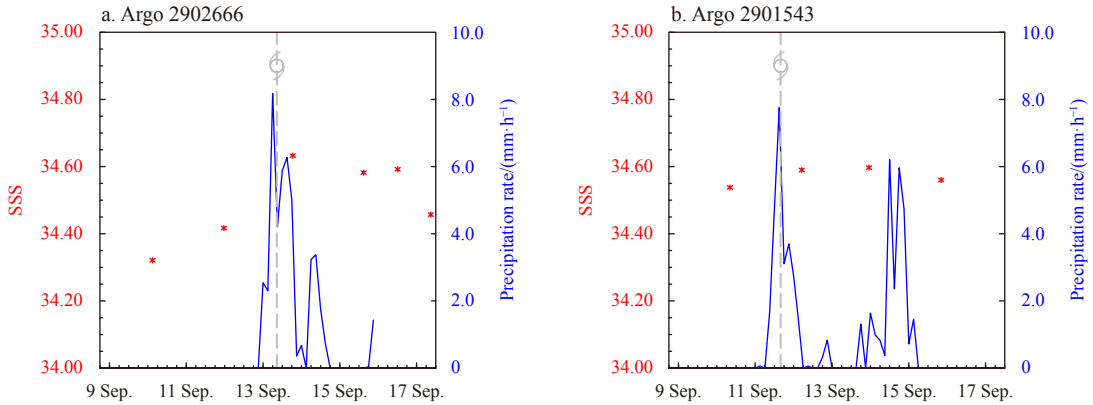

Fig. 11. Time series of Argo sea surface salinity (SSS, red asterisks) and TMI precipitation rate (blue lines).

supported that the SSS change is more likely to be controlled by oceanic vertical mixing rather than the surface freshwater forcing. Therefore the results weighted more on the internal ocean dynamics versus surface freshwater forcing on the SSS evolution.

References

Adler R F, Rodgers E B. 1977. Satellite-observed latent heat release in a tropical cyclone. Monthly Weather Review, 105(8): 956–963, doi: 10.1175/1520-0493(1977)105<0956:SOLHRI>2.0.CO;2

Bao Jianwen. 2016. Physical processes in tropical cyclone models. In: Mohanty U C, Gopalakrishnan S G, eds. Advanced Numerical Modeling and Data Assimilation Techniques for Tropical Cyclone Prediction. Dordrecht: Springer, 107–144

Cao Anzhou, Guo Zheng, Song Jinbao, et al. 2018. Near-inertial waves and their underlying mechanisms based on the South China Sea Internal Wave Experiment (2010–2011). Journal of Geophysical Research: Oceans, 123(7): 5026–5040, doi: 10.1029/2018JC013753

Cassity M M, Colgan S G. 1973. An automated objective technique for constructing tropical cyclone best tracks. Monthly Weather Review, 101(11): 824–829, doi: 10.1175/1520-0493(1973)101<0824:AAOTFC>2.3.CO;2

Chang Y C, Chen G Y, Tseng R S, et al. 2013. Observed near-surface flows under all tropical cyclone intensity levels using drifters in the northwestern Pacific. Journal of Geophysical Research: Oceans, 118(5): 2367–2377, doi: 10.1002/jgrc.20187

Chang L, He X F. 2011. InSAR atmospheric distortions mitigation: GPS observations and NCEP FNL data. Journal of Atmospheric and Solar-Terrestrial Physics, 73(4): 464–471, doi: 10.1016/j.jastp.2010.11.003

Chen S L, Polton J A, Hu J Y, et al. 2015. Local inertial oscillations in the surface ocean generated by time-varying winds. Ocean Dynamics, 65(12): 1633–1641, doi: 10.1007/s10236-015-0899-6

Cione J J. 2015. The relative roles of the ocean and atmosphere as revealed by buoy air-sea observations in hurricanes. Monthly Weather Review, 143(3): 904–913, doi: 10.1175/MWR-D-13-00380.1

Cummings J A. 2005. Operational multivariate ocean data assimilation. Quarterly Journal of the Royal Meteorological Society, 131(613): 3583–3604, doi: 10.1256/qj.05.105

Cummings J A, Smedstad O M. 2013. Variational data assimilation for the global ocean. In: Park S, Xu L, eds. Data Assimilation for Atmospheric, Oceanic and Hydrologic Applications (Vol. II). Berlin, Heidelberg: Springer, 303–343

Dee D P, Uppala S M, Simmons A J, et al. 2011. The ERA-Interim reanalysis: configuration and performance of the data assimilation system. Quarterly Journal of the Royal Meteorological Society, 137(656): 553–597, doi: 10.1002/qj.828

Emanuel K. 2003. Tropical cyclones. Annual Review of Earth and Planetary Sciences, 31: 75–104, doi: 10.1146/annurev.earth.31.100901.141259

Fu L L, Lee T, Liu W T, et al. 2018. 50 years of satellite remote sensing of the ocean. Meteorological Monographs, 59(1): 5.1–5.46, doi: 10.1175/AMSMONOGRAPHS-D-18-0010.1

Guan Shoude, Liu Ze, Song Jinbao, et al. 2017. Upper ocean response to super typhoon Tembin (2012) explored using multiplatform satellites and Argo float observations. International Journal of Remote Sensing, 38(18): 5150–5167, doi: 10.1080/01431161.2017.1335911

Guan Shoude, Zhao Wei, Huthnance J, et al. 2014. Observed upper ocean response to typhoon Megi (2010) in the Northern South China Sea. Journal of Geophysical Research: Oceans, 119(5): 3134–3157, doi: 10.1002/2013JC009661

Hawkins J D, Black P G. 1983. SEASAT scatterometer detection of gale force winds near tropical cyclones. Journal of Geophysical Research: Oceans, 88(C3): 1674–1682, doi: 10.1029/JC088iC03p01674

He Hailun, Wu Qiaoyan, Chen Dake, et al. 2018. Effects of surface waves and sea spray on air-sea fluxes during the passage of Typhoon Hagupit. Acta Oceanologica Sinica, 37(5): 1–7, doi: 10.1007/s13131-018-1208-2

Holland G J. 1980. An analytic model of the wind and pressure profiles in hurricanes. Monthly Weather Review, 108(8): 1212–1218, doi: 10.1175/1520-0493(1980)108<1212:AAMOTW>2.0.CO;2

Hong Xiaodong, Chang S W, Raman S, et al. 2000. The interaction between hurricane Opal (1995) and a warm core ring in the Gulf of Mexico. Monthly Weather Review, 128(5): 1347–1365, doi: 10.1175/1520-0493(2000)128<1347:TIBHOA>2.0.CO;2

Jin Shaohui, Li Xiaofeng, Yang Xiaofeng, et al. 2019. Identification of tropical cyclone centers in SAR Imagery based on template matching and particle swarm optimization algorithms. IEEE Transactions on Geoscience and Remote Sensing, 57(1): 598–608, doi: 10.1109/TGRS.2018.2863259

Jones W L, Cardone V J, Pierson W J, et al. 1999. NSCAT high-resolution surface wind measurements in typhoon Violet. Journal of Geophysical Research: Oceans, 104(C5): 11247–11259, doi: 10.1029/1998JC900107

Kalnay E, Kanamitsu M, Kistler R, et al. 1996. The NCEP/NCAR 40-year reanalysis project. Bulletin of the American Meteorological Society, 77(3): 437–472, doi: 10.1175/1520-0477(1996)077<0437:TNYRP>2.0.CO;2

Kishtawal C M. 2016. Use of satellite observations in tropical cyclone studies. In: Mohanty U C, Gopalakrishnan S G, eds. Advanced Numerical Modeling and Data Assimilation Techniques for Tropical Cyclone Prediction. Dordrecht: Springer, 35–47

Knaff J A, Brown D P, Courtney J, et al. 2010. An evaluation of dvorak techniquebased tropical cyclone intensity estimates. Weather and Forecasting, 25(5): 1362–1379, doi: 10.1175/2010WAF2222375.1

Knapp K R, Kruk M C, Levinson D H, et al. 2010. The international best track archive for climate stewardship (IBTrACS): Unifying

tropical cyclone data. Bulletin of the American Meteorological Society, 91(3): 363–376, doi: 10.1175/2009BAMS2755.1

Lee D K, Niiler P P. 1998. The inertial chimney: The near-inertial energy drainage from the ocean surface to the deep layer. Journal of Geophysical Research: Oceans, 103(C4): 7579–7591, doi: 10.1029/97JC03200

Li F N, Song J B, He H L, et al. 2016. Assessment of surface drag coefficient parameterizations based on observations and simulations using the Weather Research and Forecasting model. Atmospheric and Oceanic Science Letters, 9(4): 327–336, doi: 10.1080/16742834.2016.1196105

Moon I J, Ginis I, Hara T, et al. 2007. A physics-based parameterization of air-sea momentum flux at high wind speeds and its impact on hurricane intensity predictions. Monthly Weather Review, 135(8): 2869–2878, doi: 10.1175/MWR3432.1

Nilsson J. 1995. Energy flux from traveling hurricanes to the oceanic internal wave field. Journal of Physical Oceanography, 25(4): 558–573, doi: 10.1175/1520-0485(1995)025<0558:EFFTHT>2.0.CO;2

Price J F. 1981. Upper ocean response to a hurricane. Journal of Physical Oceanography, 11(2): 153–175, doi: 10.1175/1520-0485(1981)011<0153:UORTAH>2.0.CO;2

Pun I F, Chang Y T, Lin I I, et al. 2011. Typhoon-ocean interaction in the Western North Pacific: Part 2. Oceanography, 24(4): 32–41, doi: 10.5670/oceanog.2011.92

Qiu Bo. 1999. Seasonal eddy field modulation of the north pacific subtropical countercurrent: TOPEX/oseidon observations and theory. Journal of Physical Oceanography, 29(10): 2471–2486, doi: 10.1175/1520-0485(1999)029<2471:SEFMOT>2.0.CO;2

Reynolds R W, Smith T M, Liu Chunying, et al. 2007. Daily high-resolution-blended analyses for sea surface temperature. Journal of Climate, 20(22): 5473–5496, doi: 10.1175/2007JCLI1824.1

Shay L K, Goni G J, Black P G. 2000. Effects of a warm oceanic feature on hurricane Opal. Monthly Weather Review, 128(5): 1366–1383, doi: 10.1175/1520-0493(2000)128<1366:EOAWOF>2.0.CO;2

Sun Jia, He Hailun, Hu Xiaomin, et al. 2019. Numerical simulations of typhoon Hagupit (2008) using WRF. Weather and Forecasting, 34(4): 999–1015, doi: 10.1175/WAF-D-18-0150.1

Uppala S M, Kållberg P W, Simmons A J, et al. 2005. The ERA-40 reanalysis. Quarterly Journal of the Royal Meteorological Society, 131(612): 2961–3012, doi: 10.1256/qj.04.176

Velden C, Harper B, Wells F, et al. 2006. The Dvorak tropical cyclone intensity estimation technique: A satellite-based method that has endured for over 30 years. Bulletin of the American Meteorological Society, 87(9): 1195–1210, doi: 10.1175/BAMS-87-9-1195

Wada A, Kanada S, Yamada H. 2018. Effect of air-sea environmental conditions and interfacial processes on extremely intense typhoon Haiyan (2013). Journal of Geophysical Research: Atmospheres, 123(18): 10379–10405

Wada A, Uehara T, Ishizaki S. 2014. Typhoon-induced sea surface cooling during the 2011 and 2012 typhoon seasons: Observational evidence and numerical investigations of the sea surface cooling effect using typhoon simulations. Progress in Earth and Planetary Science, 1: 11, doi: 10.1186/2197-4284-1-11

Webster P J, Holland G J, Curry J A, et al. 2005. Changes in tropical cyclone number, duration, and intensity in a warming environment. Science, 309(5742): 1844–1846, doi: 10.1126/science.1116448

Yablonsky R M, Ginis I. 2009. Limitation of one-dimensional ocean models for coupled hurricane-ocean model forecasts. Monthly Weather Review, 137(12): 4410–4419, doi: 10.1175/2009MWR2863.1

Yue Xinxin, Zhang Biao, Liu Guoqiang, et al. 2018. Upper ocean response to typhoon Kalmaegi and Sarika in the South China Sea from multiple-satellite observations and numerical simulations. Remote Sensing, 10(2): 348

Zhang Qiang, Wu Liguang, Liu Qiufeng. 2009. Tropical cyclone damages in China 1983–2006. Bulletin of the American Meteorological Society, 90(4): 489–496, doi: 10.1175/2008BAMS2631.1

Zhao Biao, Qiao Fangli, Cavaleri L, et al. 2017. Sensitivity of typhoon modeling to surface waves and rainfall. Journal of Geophysical Research: Oceans, 122(3): 1702–1723, doi: 10.1002/2016JC012262

Appendix A: Bulk formula for wind stress

For typical 10-m wind speed (U_{10}), the wind stress (τ, or air-sea momentum flux) are determined by the bulk formula as

$$\tau = \rho_a C_{\mathrm{d}} {U_{10}}^2, \tag{A1}$$

where C_{d} is the corresponding drag coefficient. Here we adopt Moon et al.'s (2007) scheme for C_{d} as

$$C_{\mathrm{d}} = \kappa^2 \left(\ln \frac{10}{z_0} \right)^{-2}, \tag{A2}$$

where κ is the von Karman constant, and z_0 is roughness length which can be expressed as a function of wind speed. When $U_{10} \leqslant 12.5$ m/s,

$$z_0 = 0.018\ 5\left(0.001{U_{10}}^2 + 0.028U_{10}\right)^2/g, \tag{A3}$$

where g is the gravitational acceleration. And when $U_{10} > 12.5$ m/s,

$$z_0 = (0.085U_{10} - 0.58) \times 10^{-3}. \tag{A4}$$

Appendix B: Idealized wind vortex of tropical cyclone

Following Holland (1980) and Yablonsky and Ginis (2009), we build the idealized wind field of tropical cyclone as

$$V_{\mathrm{c}} = [AB\,(p_{\mathrm{n}} - p_{\mathrm{c}})\,\mathrm{e}^{-A/r^B}/\rho_a r^B]^{1/2}, \tag{B1}$$

$$R_{\max} = A^{1/B}, \tag{B2}$$

$$v_{\max} = (B/\rho \mathrm{e})^{1/2}(p_{\mathrm{n}} - p_{\mathrm{c}})^{1/2}. \tag{B3}$$

where V_{c} is the wind speed, r is the radius, $v_{\max}$ is the maximum sustain wind of tropical cyclone, A and B are shape parameters, p_{n} is the ambient pressure, p_{c} is the central pressure and ρ_{a} is air density. The geostrophic wind V_{c} is then converted to surface wind with constant coefficient (0.8).